

Article

Operation of a Hybrid Energy Storage System Based on a Cascaded Multi-Output Multilevel Converter with a Carrier-Based Modulation Scheme

Fidel Figueroa ¹, Ricardo Lizana Fuentes ^{1,*} , Stefan M. Goetz ^{2,3}  and Sebastian Rivera ^{1,4} 

¹ Department of Electrical Engineering, Centro de Energía, Universidad Católica de la Santísima Concepción, Concepción 4090541, Chile; ffigueroa@ucsc.cl (F.F.)

² Department of Engineering, University of Cambridge, Cambridge CB3 0FA, UK; stefan.goetz@duke.edu

³ Department of Electrical Engineering, Duke University, Durham, NC 27710, USA

⁴ DCE&S Group, Department of Electrical Sustainable Energy, Delft University of Technology, 2628 CD Delft, The Netherlands

* Correspondence: ricardolizana@ucsc.cl

Abstract: Hybrid Energy Storage Systems (HESSs) have gathered considerable interest due to their potential to achieve high energy and power density by integrating different storage technologies, such as batteries and capacitors, to name a few. Among the various topologies explored for HESSs, the multi-output multilevel converter stands out as a promising option, offering decoupled operation of the AC ports while maintaining an internal balance among the diverse storage units. In this paper, the operation and restrictions of a HESS based on a multi-output multilevel converter with a carrier-based modulation scheme are presented. The study provides compelling evidence of the correct operation of the proposed modulation scheme and highlights its advantages, including simplicity and stability.

Keywords: hybrid energy storage systems; multi-output multilevel converters; carrier-based modulation scheme



Citation: Figueroa, F.; Lizana Fuentes, R.; Goetz, S.M.; Rivera, S. Operation of a Hybrid Energy Storage System Based on a Cascaded Multi-Output Multilevel Converter with a Carrier-Based Modulation Scheme. *Energies* **2023**, *16*, 7150. <https://doi.org/10.3390/en16207150>

Academic Editor: Alon Kuperman

Received: 5 September 2023

Revised: 5 October 2023

Accepted: 11 October 2023

Published: 19 October 2023



Copyright: © 2023 by the authors. Licensee MDPI, Basel, Switzerland. This article is an open access article distributed under the terms and conditions of the Creative Commons Attribution (CC BY) license (<https://creativecommons.org/licenses/by/4.0/>).

1. Introduction

Energy storage systems are being called on to take a leading role in the modernization of electric grids [1–4]. The extensive incorporation of renewable energy sources (RES) along with the deeper electrification of industry processes imposes important challenges to the electric power grid [5–11], and a large presence of energy storage systems (ESSs) can alleviate this transition. However, electric facilities, namely generation and distribution centers, are not typically designed to incorporate storage, leading to several drawbacks. Moreover, the complexity of matching generation and consumption is increasing given the reduced inertia in a power-electronics-dominated grid [2,12,13]. In order to improve the controllability, smooth the demand response, and reduce energy waste and also the need for grid reinforcements, ESSs are essential assets in the modern electric grid [13–17].

On the other hand, ESSs are also crucial in the microgrid concept, which has been developed over recent decades to accommodate fast-changing loads and generators in the electric grid [18–20]. This clusterization of electric systems into controllable and detachable blocks by means of power electronics permits a distributed integration of RESs, ESSs, and loads with independence from the electric power grid. Hence, the development of new integrated power converters and energy storage units remains one of the key aspects in the upcoming electric system. In order to further improve the ESSs' capabilities, different storage technologies can be combined in the shape of hybrid ESSs. By mixing ultra-capacitors, capacitors and batteries, and even non-electricity-based storage mechanisms, different features can be exploited depending on the scenario, for instance, high energy and high power density [21,22].

The key to achieving the correct operation of a HESS is the power electronic topology. Indeed, different power topologies for HESSs are reported in the literature that enable both an AC grid connection and a balanced operation of the different energy storage sources integrated into the converter. Voltage source converters (VSC) based on a modular structure, such as cascaded H-bridge (CHB) or modular multilevel converters (MMC), appear in the literature as promising solutions for the integration HESSs into the system, taking advantage of the configuration for these converters and assigning different power modules of the structure to each storage element, while using control and modulation strategies to balance the system [23,24]. Moreover, the multilevel nature of these converters is also beneficial for other aspects such as significant filter reduction and redundancy in case of failure [25–27].

On the other hand, cascaded dual-output multilevel (CDOM) converters are an interesting alternative for interfacing HESSs. The core idea of CDOM converters is that they can provide the ability to increase the number of output ports, which can operate in a decoupled manner and with multilevel waveforms [28]. Indeed, in Ref. [17], it is shown how it is also possible to scale this system so that each of the system outputs can feature a multilevel voltage waveform, while also ensuring the internal balance of the different types of energy storage elements, implementing a CDOM-HESS.

However, in most papers based on the operation of CDOMs, the CDOMs are controlled by model predictive control strategies (MPC), which implies a distributed spectrum of voltage harmonics in each of the output ports [17,29,30]. This can be a sensible drawback for grid-tied applications because the use of LC or LCL filters is very common when the converters are connected to the grid in order to ensure a harmonic spectrum that complies with current regulations in each zone. However, the use of these filters imposes an important restriction on the resonance frequency, so it is key to define modulation forms that allow for ensuring a concentrated harmonic spectrum and that avoid difficulties in the excitation of harmonic resonant modes.

In this paper, a carrier-based modulation scheme for a HESS based on a cascaded multi-output multilevel converter is presented. The main concept is to achieve an internal balance of the storage units and generate multilevel waveforms across the AC output of the proposed system with a carrier-based modulation scheme and a predefined harmonic spectrum of the output waveforms.

2. Converter Topology Analysis

The cascaded multi-output multilevel (CMOM) converter will act as an interface for the HESS. As depicted in [28], CMOM converters comprise m stages that can enable n output ports that are decoupled up to a certain point. When the CMOM is operating in the stable operation region, each of these n voltage outputs can synthesize voltage signals with $2m+1$ levels, with arbitrary amplitude, frequency, and phase angle. Additionally, the converter offers a simpler mechanism to balance the DC voltages among the cells. These features allow the incorporation of e energy storage units to the converter structure, with the particularity that these units can be heterogeneous in terms of technology, dynamics, and so on.

As displayed in Figure 1, the CMOM converter topology in this work considers $m = 2$ with $n = 2$. The idea is to propose a carrier-based modulation scheme for the topology introduced in [17], since a defined harmonic content can be beneficial for minimizing resonances in the system, especially given the parallelization of cells enabled by the modular multilevel series parallel converter (MMSPC) modules [31]. Hence, the power converter features the use of a single battery while achieving five voltage-level waveforms in each port. The remaining H-bridge of the MMSPC cell in the converter uses a capacitor, which needs to keep its voltage balanced with the battery unit to allow the correct operation of the system. This modulation scheme is developed in such a way that connects the modules both in series and in parallel, inherently keeping the voltage balance between the storage units and also maintaining a high quality in the AC output ports. Moreover, the scheme

also reduces the current spikes during parallelization in order to achieve a similar efficiency to the method discussed in [17].

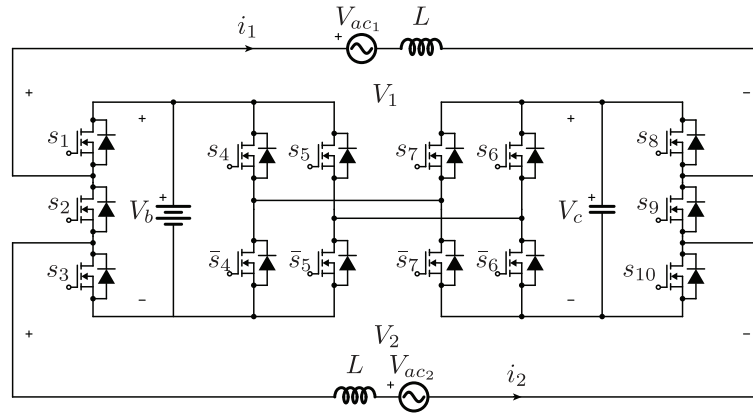


Figure 1. Cascaded multi-output multilevel converter description.

As presented in Figure 1, the converter comprises 14 semiconductors and two energy storage units, namely a battery and a capacitor. As discussed earlier, this structure allows the generation of two decoupled AC outputs (V_1 and V_2). The system can be connected to two AC systems, where each one is modeled by a non-ideal inductive filter and a single-phase AC supply (V_{ac_x} , where $x = \{1, 2\}$).

To achieve the inherent internal voltage balance between the battery and the capacitor implemented in the system, a configuration based on two H-bridges is used (denoted by semiconductors s_4, s_5, s_6, s_7 and their respective negatives), which, through the modulation stage, prioritize the switching states that allow these units to be connected in parallel.

In this way, an internal voltage balance is achieved between these units without the need to implement complex control loops, nor are additional current or voltage sensors required. This solution has been validated in different documents [32–38], and if this modulation strategy is correctly implemented, it can be ensured that $V_b = V_c = v_{dc}$ is met. Table 1 summarizes the available switching states and the voltages at each of the converter outputs.

Table 1. Switching states and output voltages.

s_1	s_2	s_3	s_4	s_5	s_6	s_7	s_8	s_9	s_{10}	V_1	V_2	$ \Delta v_{dc} $
1	0	1	0	1	1	0	1	0	1	0	0	0
1	1	0	0	1	1	0	1	0	1	0	v_{dc}	v_{dc}
1	0	1	0	1	1	0	1	1	0	0	$-v_{dc}$	v_{dc}
1	0	1	0	1	1	0	0	1	1	v_{dc}	0	v_{dc}
1	1	0	1	0	0	1	0	1	1	v_{dc}	v_{dc}	0
1	1	0	0	0	1	1	1	0	1	v_{dc}	$2v_{dc}$	v_{dc}
1	0	1	0	0	1	1	0	1	1	$2v_{dc}$	v_{dc}	v_{dc}
1	1	0	0	0	1	1	0	1	1	$2v_{dc}$	$2v_{dc}$	0
0	1	1	0	1	1	0	1	0	1	$-v_{dc}$	0	v_{dc}
0	1	1	1	0	0	1	1	1	0	$-v_{dc}$	$-v_{dc}$	0
1	0	1	1	1	0	0	1	1	0	$-v_{dc}$	$-2v_{dc}$	v_{dc}
0	1	1	1	1	0	0	1	0	1	$-2v_{dc}$	$-v_{dc}$	v_{dc}
0	1	1	1	1	0	0	1	1	0	$-2v_{dc}$	$-2v_{dc}$	0

3. Pulse Width Modulation Approach for Cascaded Multi-Output Multilevel Converters

This paper implements a carrier-based modulation scheme given its simplicity and lower computational complexity with respect to other modulation strategies, such as space vector modulation or finite state MPC (FS-MPC) [39]. Moreover, with the implementation of a carrier-based modulation scheme, it is possible to handle the harmonics generated by the converter directly in order to optimize the filter sizes since their location in the spectrum is known a priori.

The control block diagram of a CMOM converter is shown in Figure 2, where different stages are proposed in order to assure the correct operation of both the AC output generated by the CMOM topology as well as the balancing of the internal capacitor voltage.

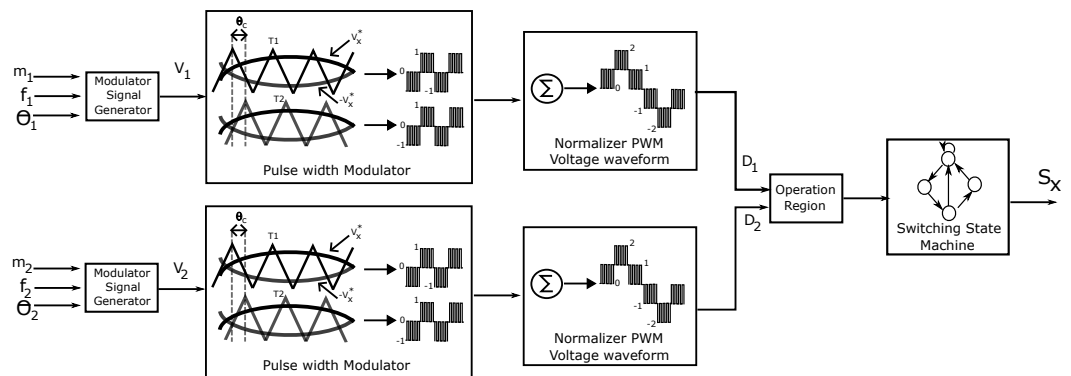


Figure 2. Control scheme of a cascaded multi-output multilevel converter.

3.1. Modulator Signal Generator

The first stage of the proposed modulation scheme presented in Figure 2 allows the modulating signal for the AC output voltages V_1 and V_2 to be generated, created by the converter. This signal is defined by:

$$V_x^* = m_x \cdot \sin(2\pi f_x + \theta_x) \quad (1)$$

where $x = 1, 2$ refer to the AC outputs of the converter. The amplitude modulation index (m_x), the output frequency (f_x), and the phase (θ_x) are determined by the operational requirements in each AC output of the converter.

3.2. Pulse Width Modulation

The modulation signals defined for both AC outputs are processed in a carrier-based modulation stage. An important degree of freedom provided by the proposed modulation strategy is that it is flexible to any carrier-based modulation scheme. In this proposal, a phase-shifted PWM (PS-PWM) modulation strategy will be used. Figure 2 shows the implementation of a unipolar PS-PWM strategy, in which the voltage references for the AC systems 1 and 2 are compared with two triangular carrier signals (T1 and T2). The results of this comparison are two normalized voltage signals with three voltage levels. The phase shift between the carriers, considering $m = 2$, is defined by

$$\theta_c = \frac{\pi}{m} = \frac{\pi}{2} \quad (2)$$

3.3. PWM Voltage Waveform Normalizer

The outputs of each comparison of the PWM stage are added together, which results in a normalized voltage waveform (D_x). The D_x signal consists of the definition of the five normalized voltage levels of the proposed topology ($-2, -1, 0, 1, 2$) for each output of the topology. Then, the normalized voltage waveform (D_x) of both AC outputs are evaluated to corroborate if the system is operating in the stable operation region.

3.4. Operation Region

The AC systems have a restricted operation point, which depends on the maximum modulation index that can be achieved. However, in CMOM converters, there is a second factor that limits the operation region, and it is linked to the difference between the normalized waveforms D_1 and D_2 .

The difference between D_1 and D_2 is defined by the expression Δv_{dc} :

$$\Delta v_{dc} = |D_1| - |D_2| \quad (3)$$

From Table 1, it is possible to deduce that the maximum $|\Delta v_{dc}|$ is the rated battery voltage ($|\Delta v_{dc}| = |V_1 - V_2|$). Then, assuming a correct balancing offered by the modulation scheme, this maximum difference is simply v_{dc} (i. e., $V_b = V_c = v_{dc}$). Thus, the maximum deviation expression is defined by:

$$|\Delta v_{dc}|_{max} = v_{dc} \quad (4)$$

Hence, if the references defined in (1) for V_1 and V_2 fall outside the stable operating region of the system presented in (4), these will be limited in order to ensure there is no over-modulation.

3.5. Switching State Machine

Each normalized voltage waveform (D_x) is correlated with the output voltage V_x . To directly choose the switching state required to generate the output voltage V_x , Table 1 is used to select the state that matches the voltage levels defined in V_x . Note that the importance of the inclusion of the operation region definition stage is to ensure that the switching states to be selected correspond to those defined in the Table 1 and that there is no over-modulation. Moreover, in order to give flexibility to the modulation system, redundant states could be selected in order to reduce the switching losses or distribute the losses in the different semiconductors of the system in a more homogeneous way, depending on the application of the proposed system.

4. Simulation Results

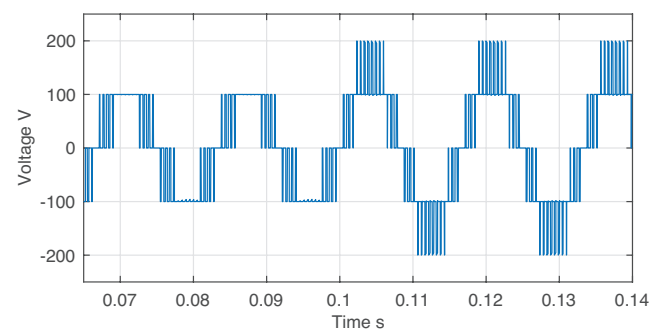
To verify the correct operation of the proposed modulation, different simulations are carried out in PLECS[®] software using the parameters defined in Table 2. The objective is to test the decoupled operation of each AC port with the proposed modulation scheme.

Table 2. Simulation parameters.

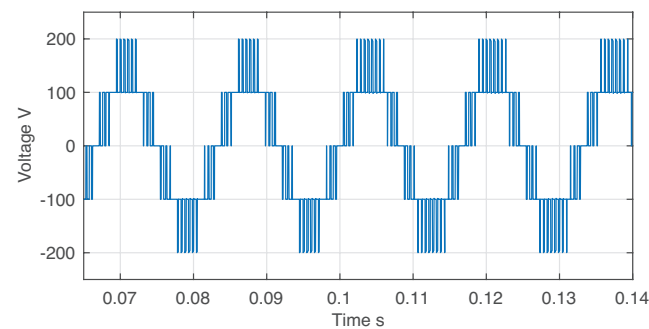
Parameter	Value
Inductance system 1 and 2 (L)	15 [mH]
Resistance system 1 and 2 (R)	10 [Ω]
Inductance system 1 and 2 Section 4.5 (L)	9.6 [mH]
Resistance system 1 and 2 Section 4.5 (R)	0.1 [Ω]
AC Grid 1 amplitude (V_{ac1}) Section 4.5	150 [V]
AC Grid 2 amplitude (V_{ac2}) Section 4.5	150 [V]
AC Grid 1 frequency Section 4.5	60 [Hz]
AC Grid 2 frequency Section 4.5	60 [Hz]
Battery voltage (v_{dc})	100 [V]
Capacitance (C)	1000 [μ F]
PWM carrier frequency (f_c)	480 [Hz]
PWM carrier frequency (f_c) Section 4.5	1200 [Hz]

4.1. Operation with Different Modulation Index Amplitudes

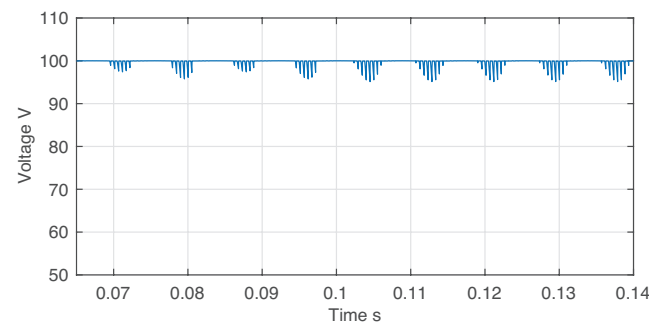
In Figure 3, the operation with different modulation indices for each AC voltage output is shown. Figure 3a demonstrates the operation of the AC output voltage 1 with a amplitude of the modulation index of $m_1 = 0.5$. In $t = 0.1$ s, the amplitude of the modulation index changes to $m_1 = 0.7$. Therefore, it is possible to appreciate from Figure 3a a change in the voltage levels present in V_{ac1} , reflecting a larger fundamental amplitude being generated in this port. The normalized fundamental component for the voltage in AC system 2 m_2 is kept constant at 0.7, and therefore, the AC voltage 2 maintains the 5-level voltage waveform throughout the test, as displayed in Figure 3b. Please note that the system is operating in the stable operation region, hence leading to a decoupled operation between the AC ports. Finally, Figure 3c shows the capacitor voltage V_c of the CMOM converter. It is possible to validate that the capacitor and battery voltages are kept balanced ($V_c = 100$ V) during all tests, validating the internal balance of the system maintained by the novel modulation strategy and guaranteeing the multilevel voltage pattern in each AC output of the converter. This balance also ensures a high-quality current is supplied to both systems, in addition to a well-defined spectrum pattern.



(a)



(b)



(c)

Figure 3. Simulated operation with different modulation index amplitudes: (a) AC output voltage 1 V_1 ; (b) AC output voltage 2 V_2 ; (c) capacitor voltage V_c .

4.2. Operation Mode with Different Phases

For this validation of the proposed system operation, both amplitude modulation indices are set to the same value, i.e., $m_1 = m_2 = 0.7$. However, a phase difference equal to $\Delta\theta = \pi/3$ rad is imposed.

In Figure 4a,b, both AC output voltages of the system exhibit 5-voltage levels, and it is possible to appreciate the phase difference between both voltage signals. It is important to note that this decoupled operation between both AC voltage output is possible because the references are still inside the stable operation region. Finally, in Figure 4c, the capacitor voltage balance is shown, and similar to the earlier case of Section 4.1, it presents an average value that matches battery voltage, confirming the system remains internally balanced.

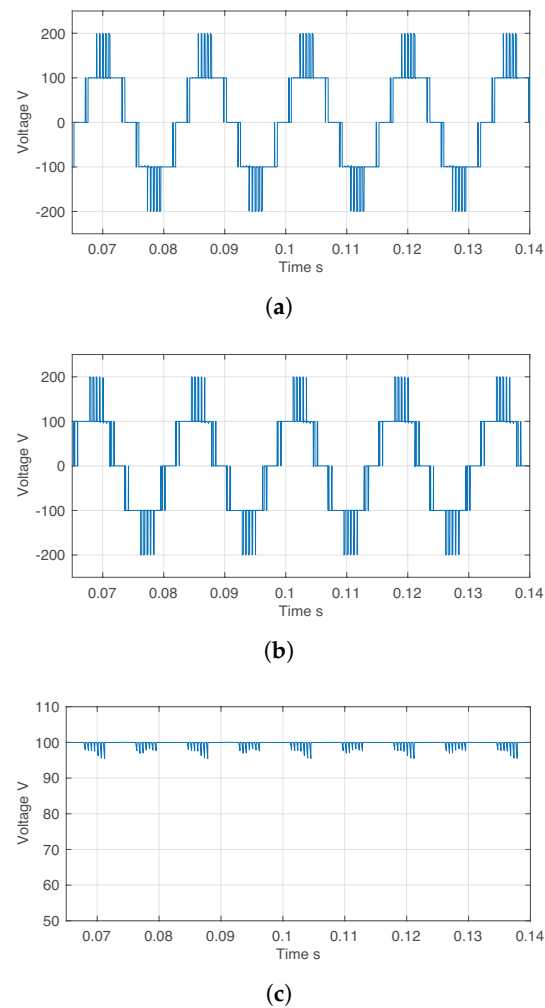


Figure 4. Simulated operation with different phases: (a) AC output voltage 1 V_1 ; (b) AC output voltage 2 V_2 ; (c) capacitor voltage V_c .

4.3. AC Voltage Harmonics Analysis

The harmonic content of the voltage generated at the converter outputs is shown in Figure 5. It is possible to appreciate how the fundamental component appears and, moreover, the set of harmonics that appear around four times the carrier frequency (f_c). This is due to the unipolar PWM modulation implemented and multiplied by the number of modules used, i.e., $f_{PWM} = m \cdot (2f_c)$. Specifically, in this work, each converter has two cells, i.e., $m = 2$, so the voltage harmonics produced by the modulation concentrate most of their energy on the side bands around $f_{PWM} = 4f_c$.

It is also important to highlight the advantage of controlling the CMOM converter with a carrier-based modulation scheme, since the harmonic content is concentrated and

not randomly distributed as with FS-MPC strategies. This result is especially important for grid-connected systems, which may include LCL-filter stages, and which have voltage harmonic spectrum limitations due to the resonant frequencies inherent to their structure.

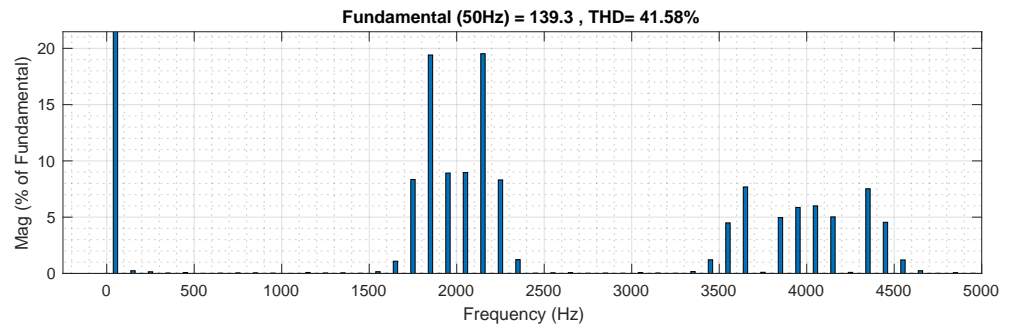


Figure 5. FFT of AC output voltage with modulation index equal to 0.7.

4.4. Power Loss Analysis

To evaluate the power losses of the multi-output converter operating with the proposed carrier-based modulation strategy, the thermal modeling tool of the PLECS[®] 4.7.5 software is used, along with the parameters presented in Table 2. Also, the CMOM is built using the SCT4045DR Silicon Carbide from Rohm, and they are hard commutated.

To verify the losses of the converter, the semiconductors of the topology presented in Figure 1 are divided into four groups. Semiconductors $s_1, s_2,$ and s_3 and $s_8, s_9,$ and s_{10} correspond to the three switch cells (TS) that are connected at the ends of the system, which are labeled as TS1 and TS2, respectively. Then, semiconductors s_4, s_5 and s_6, s_7 (and their respective complementary devices) correspond to the internal H-bridge (HB) configuration of the system, which are grouped as HB1 and HB2, respectively. Moreover, the modulation index for output 1 is fixed to $m_1 = 0.7$, while the modulation index of output 2 is modified to evaluate losses under different power ranges.

To present the loss distribution of the system, Figure 6 is shown. Conduction power losses of each group are shown in Figure 6a. It is possible to identify that the losses are balanced among the different groups, with a slight increase in HB1 and HB2. Concerning the switching losses, these are presented in Figure 6b. In this case, again, the switches of HB1 and HB2 have higher losses. The increase in the losses of HB1 and HB2 are consequences of the carrier frequency. A lower carrier frequency produces an increase in the oscillation of the capacitor voltage and therefore decreases the efficiency of the system. However, it is important to note that it is possible to achieve a correct performance of the proposed system with a low carrier frequency in the modulation stage, and the parallel connection of the internal system is still feasible.

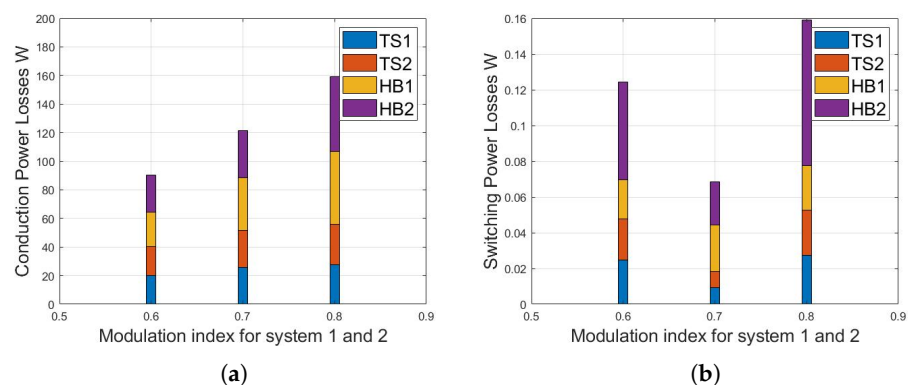


Figure 6. Distribution of power losses: (a) conduction losses; (b) switching losses.

4.5. Grid-Tied Operation

Figure 7 shows the closed-loop operation of the system tied to two AC systems in order to validate the proposed modulation and balance. For this, the AC currents of systems 1 and 2 are controlled by linear proportional integral (PI) controllers. Please also note that each AC system is composed of an inductive filter and a single-phase AC voltage supply. The inductive filter is considered non-ideal; hence, it has an inductance of 9.6 mH and also a resistance of 0.1 Ω . Also, both grids' supplies have an amplitude of 150 V and a frequency of 60 Hz.

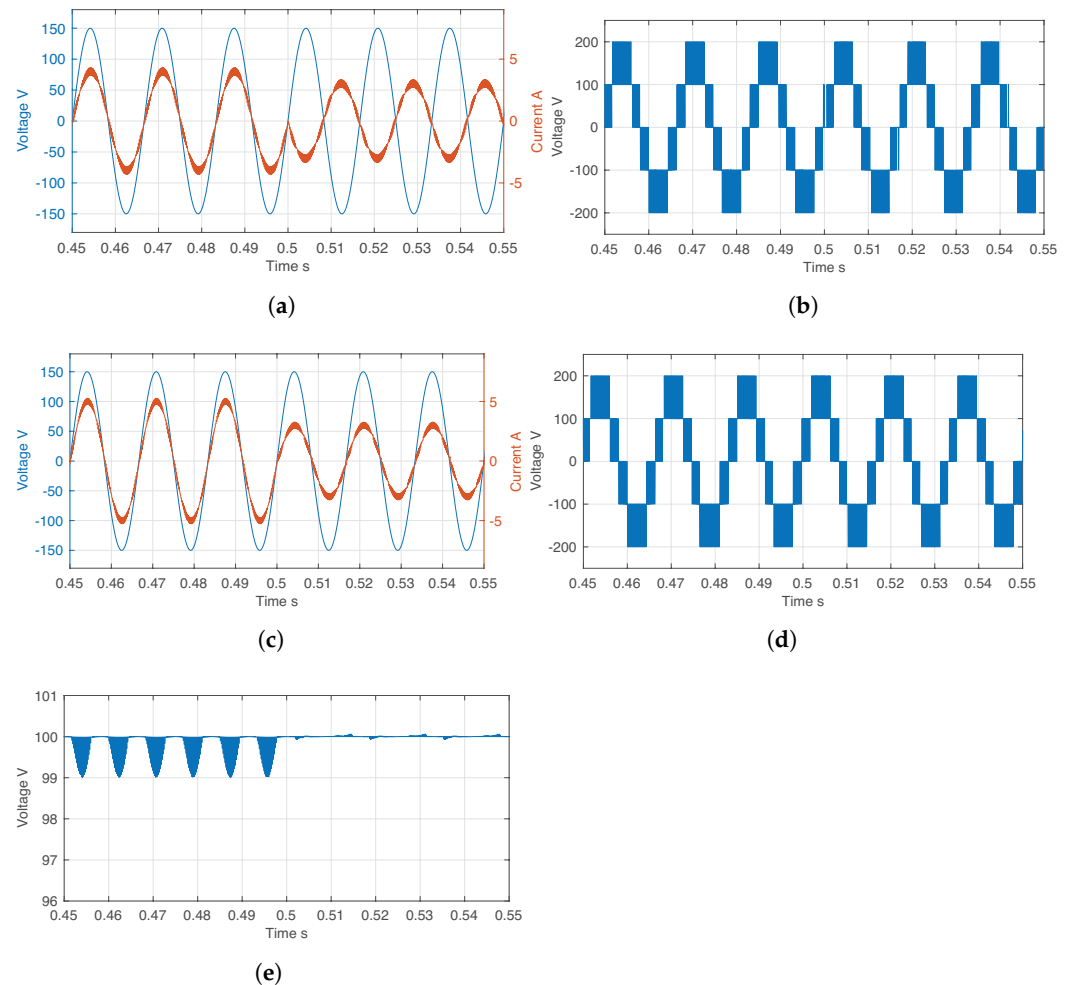


Figure 7. Grid-connected operation with current control: (a) AC current and voltage system 1. (b) Converter voltage V_1 . (c) AC current and voltage system 2. (d) Converter voltage V_2 . (e) Capacitor voltage V_c .

Initially, both AC systems present currents in phase with their corresponding voltages, and hence both grids are sinking power from the HESS, following the definition in Figure 1. Since the battery is supplying the energy, the test illustrates the bidirectional power flow capabilities of the CMOM converter in both AC output ports. From the results presented in Figure 7a–d it can be seen that current references of system 1 and 2 are, respectively, 4 A and 5 A, demonstrating the capabilities of the proposed modulation technique to maintain the outputs decoupled and sink different power levels as requested by each of the grid-connected ports.

Then, at $t = 0.5$ s, the current reference of AC system 1 changes to -3 A, while the current reference of AC system 2 changes to 3 A simultaneously. These references result in AC grid 1 supplying power into AC system 2, which complements the power being delivered by the battery. In this way, the decoupled control capacity of both currents of the

proposed system is demonstrated, in addition to further illustrating that the effectiveness of the developed modulation allows maintaining the capacitor and battery voltage balance throughout the entire simulated scenario, as shown in Figure 7e.

As a final remark, the results presented in Figure 7 also validate the high quality of the signals injected into the grid by the CMOM. Both ports are able to generate high-quality currents from the grids throughout the whole test. First, when both systems are injecting power from the HESS, each grid current presents a total harmonic distortion (THD) of 4% and 3.52%, respectively. Then, when the operation of the AC system 1 is changed into supplying power from its AC port while AC system 2 reduces the power demand from the HESS, the resulting current THDs are 5.85% and 6% (which correspond to total demand distortions (TDDs) of 3.31% and 3.6% for each system).

5. Experimental Results

The experimental results presented in this section aims to demonstrate the correct performance of the proposed modulation strategy for the CMOM converter. By validating some relevant scenarios, the applicability and versatility of the converter proposed in [17] can be demonstrated for a carrier-based modulation scheme, which can improve the list of features with a cost-effective computational burden and ease of implementation.

Considering this, two different operation condition are presented: decoupled amplitude and phase angle operation between AC output voltages for grids 1 and 2. The parameters used in the Experimental Results section are summarized in Table 3, and the experimental setup implemented is displayed in Figure 8.

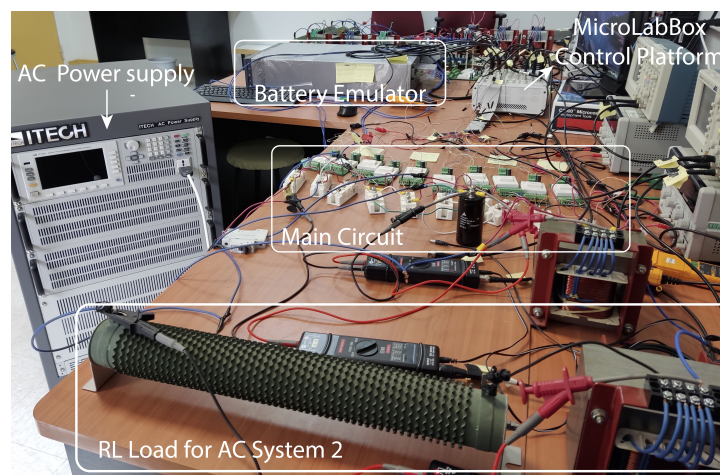


Figure 8. Cascaded multi-output multilevel converter experimental setup.

Table 3. Experimental parameters.

Parameter	Value
Inductance system 1 and 2 (L)	15 [mH]
Resistance system 1 and 2 (R)	10 [Ω]
Battery voltage (v_{dc})	20 [V]
Capacitance (C)	1000 [μ F]
Sample time (Δt)	50 [μ s]
PWM carrier frequency (f_c)	500 [Hz]

5.1. Operation Mode with Different Modulation Indices

To validate the operation modes of the system with different amplitudes of the modulating signals for systems 1 and 2, the references for AC system 1 and 2 are defined with the

same phase and frequency (50 Hz). The modulation index reference for the AC system 2 is kept controlled to an amplitude of 0.7, as is presented in Figure 9a, obtaining an AC output voltage V_2 with five voltage levels, as shown in Figure 9b. In addition, the modulation index reference of the AC system 1 is equal to 0.5, hence leading to an AC output voltage V_1 with three voltage levels, as can be seen in Figure 9b. Then, a step change in the modulation index amplitude of AC output 1 takes place, reaching a final value of 0.7. After the change, it can be seen how now V_1 exhibits a 5-voltage level waveform. In this way, the decoupled operation in both AC outputs under different modulation indices is validated.

In order to further confirm the correct operation of the modulation strategy, Figure 9c presents the capacitor voltage V_c . Considering that, in this case, the battery employed as the main energy storage element has a rated voltage of 100 V, the results demonstrate that the parallel connection between the storage units provides an effective balancing approach, allowing the voltages to remain balanced throughout the whole test.

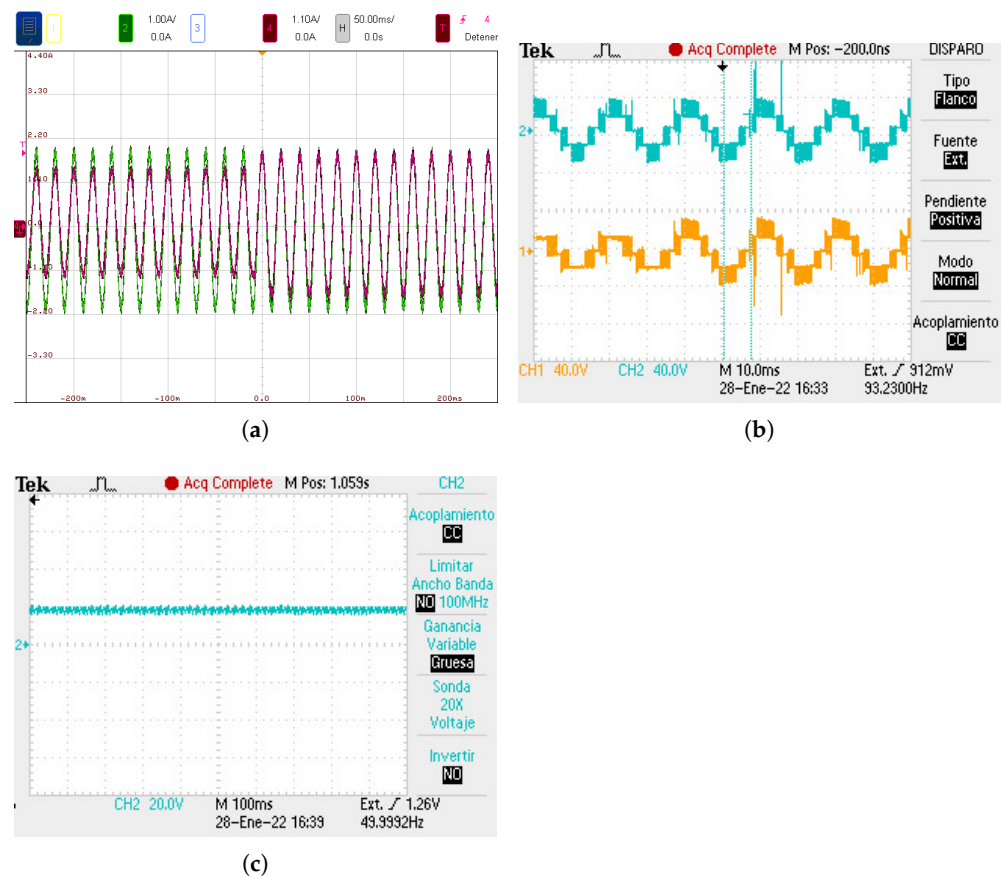


Figure 9. Operation with different modulation indices: (a) CH2: modulation signal reference for AC system 2, 1A/div; CH4: modulation signal reference for AC system 1, 1A/div. (b) CH1: converter voltage AC system 1, 40 V/div; CH2: Converter voltage AC system 2, 40 V/div; (c) Capacitor voltage, 20 V/div.

5.2. Operation Mode with Decoupled Phases

The operation of the system with different phase angles in each of the converter outputs is presented. The modulation index references for both systems are the same, $m_1 = m_2 = 0.6$, and the frequencies of both references are set to 50 Hz. The phase difference between AC systems 1 and 2 is initially set to 0 degrees. Then, a phase difference equivalent to $\Delta\theta = \pi/3$ is implemented, which can be seen in the waveforms shown in Figure 10a. The scenario is further illustrated in Figure 10b,c. The aforementioned figures present the converter voltages and the capacitor voltage, respectively. From these results, it

is possible to conclude that the system is totally stable and both systems are operating with no distortion.

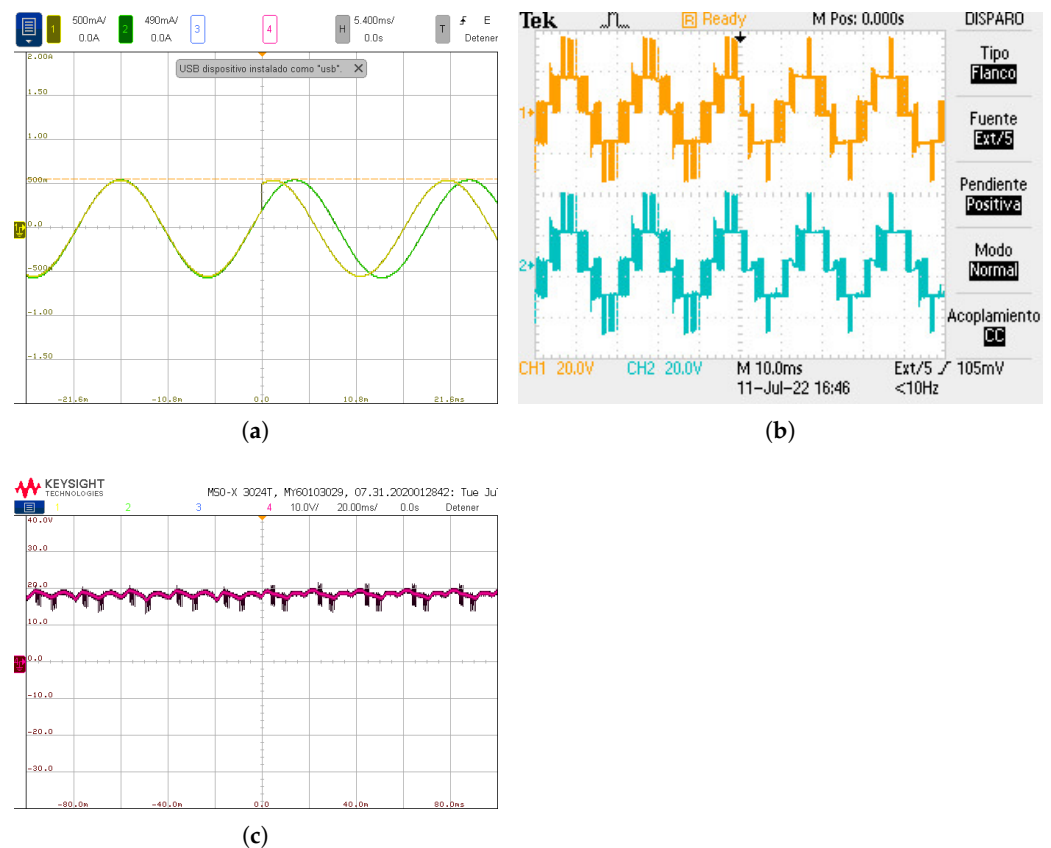


Figure 10. Operation with different phases. (a) CH2: modulation signal reference for AC system 2, 1A/div; CH4: modulation signal reference for AC system 1, 0.5 A/div. (b) CH1: converter voltage AC system 1, 20 V/div; CH2: Converter voltage AC system 2, 20 V/div. (c) Capacitor voltage, 20 V/div.

The obtained results validate the effectiveness of the proposed PWM scheme for regulating the CMOM converter with heterogeneous energy sources. This can be translated to the development of a cost-effective hybridization of multilevel single-battery energy storage systems connected to the grid, while enhancing the grid performance with a higher-quality voltage waveform. Also, this sets the ground for the extension to three-phase grids, where the minimal number of battery stages used can be also beneficial for developing a reliable and convenient way of deploying storage at different points of the grid.

5.3. Steady-State Performance

The steady-state performance of the proposed modulation scheme for the CMOM converter is analyzed in the following section. The converter is operated under normal conditions to be analyzed at different modulation indices. Figure 11 shows the THD of the output voltage. It is important to note that the results presented in Figure 11 are valid for both AC outputs (V_1 and V_2). For a higher modulation index, the number of voltage levels increases to a maximum of five steps, and therefore, the THD of the voltage is reduced significantly in both AC outputs, which benefits the quality of the current being sinked or supplied to each AC system.

Another important aspect to consider is assuming that the system is operating in a stable zone; the voltage THDs for outputs 1 and 2 can be determined from Figure 11. For example, if the modulation index of V_1 is 0.5 and the modulation index of V_2 is 0.3, the voltage THDs are 56.49% and 113.84%, respectively.

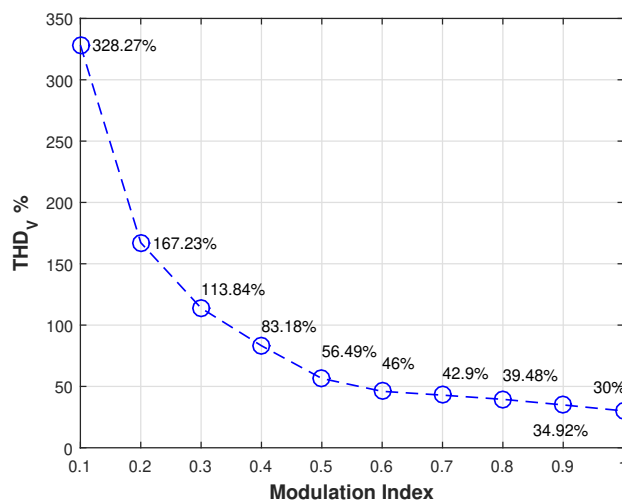


Figure 11. THD of AC output voltages 1 and 2.

6. Future Research Directions

Based on the results presented, the authors define the optimization of the states selected in Table 1 as an interesting field of research in order to use the redundant states and minimize the internal losses of the converter's semiconductors.

Another interesting aspect is the study of incorporating distributed inductances into the structure of the MMSPC-based system. This measure has proven to be effective in decreasing the losses of the system that arise whenever the parallel states are used in the proposed modulation scheme.

Finally, the balance achieved with simple carrier-based modulation schemes permits extending the single-battery hybridization approach to three-phase converters. By doing so, the hardware requirements of grid-connected HESSs can be softened, supporting their development toward cost-effectiveness and widespread use to support the large-scale deployment of RESs.

7. Conclusions

This document introduces a carrier-based modulation scheme for a hybrid ESS based on a cascaded multi-output multilevel converter. The objective of proposing a modulation based on carriers is to allow a simple and efficient way to modulate the converter, and specifically defining a defined band to locate the harmonics generated by the system, in order to facilitate the integration of LCL filters for the connection to electrical AC networks.

The simulation and experimental results validate the operation of the modulation in the CMOM converter, where it is also possible to confirm the internal balance of the energy storage elements in the system and the decoupled control of the AC output of the system.

Author Contributions: Conceptualization, F.F., R.L.F. and S.M.G.; Methodology, R.L.F.; Software, F.F.; Validation, F.F.; Formal analysis, R.L.F.; Investigation, R.L.F.; Resources, R.L.F.; Writing—original draft, R.L.F. and S.R.; Writing—review & editing, S.M.G. and S.R.; Supervision, S.R.; Project administration, R.L.F.; Funding acquisition, R.L.F. All authors have read and agreed to the published version of the manuscript.

Funding: This research was funded by the Agencia Nacional de Investigación y Desarrollo (ANID) through the following projects: Fondo Nacional de Desarrollo Científico y Tecnológico (FONDECYT) under Grant 1230306, the Advanced Center of Electrical and Electronic Engineering (AC3E) under Grant ANID/Basal/FB0008, and the Solar Energy Research Center (SERC) Chile under Grant ANID/FONDAP/1522A0006. Also, financial support by the Universidad Católica de la Santísima Concepción through the program Fondo de Actividades Académicas is greatly acknowledged.

Data Availability Statement: The data presented in this study are available on request from the corresponding author.

Conflicts of Interest: The authors declare no conflict of interest

References

1. Stecca, M.; Elizondo, L.R.; Soeiro, T.B.; Bauer, P.; Palensky, P. A Comprehensive Review of the Integration of Battery Energy Storage Systems Into Distribution Networks. *IEEE Open J. Ind. Electron. Soc.* **2020**, *1*, 46–65. [[CrossRef](#)]
2. Stynski, S.; Luo, W.; Chub, A.; Franquelo, L.G.; Malinowski, M.; Vinnikov, D. Utility-Scale Energy Storage Systems: Converters and Control. *IEEE Ind. Electron. Mag.* **2020**, *14*, 32–52. [[CrossRef](#)]
3. Xue, W.; Wang, Y.; Chen, Z.; Liu, H. An integrated model with stable numerical methods for fractured underground gas storage. *J. Clean. Prod.* **2023**, *393*, 136268. doi:10.1016/j.jclepro.2023.136268. [[CrossRef](#)]
4. Blatsi, Z.; Judge, P.D.; Finney, S.J.; Merlin, M.M.C. Blackstart Capability of Modular Multilevel Converters From Partially-Rated Integrated Energy Storage. *IEEE Trans. Power Deliv.* **2023**, *38*, 268–276. [[CrossRef](#)]
5. Schrittwieser, L.; Kolar, J.W.; Soeiro, T.B. 99% Efficient three-phase buck-type SiC MOSFET PFC rectifier minimizing life cycle cost in DC data centers. *CPSS Trans. Power Electron. Appl.* **2017**, *2*, 47–58. [[CrossRef](#)]
6. Rothmund, D.; Guillod, T.; Bortis, D.; Kolar, J.W. 99% Efficient 10 kV SiC-Based 7 kV/400 V DC Transformer for Future Data Centers. *IEEE J. Emerg. Sel. Top. Power Electron.* **2019**, *7*, 753–767. [[CrossRef](#)]
7. Marzooghi, H.; Garmroodi, M.; Verbič, G.; Ahmadyar, A.S.; Liu, R.; Hill, D.J. Scenario and Sensitivity Based Stability Analysis of the High Renewable Future Grid. *IEEE Trans. Power Syst.* **2022**, *37*, 3238–3248. [[CrossRef](#)]
8. Rivera, S.; Goetz, S.M.; Kouro, S.; Lehn, P.W.; Pathmanathan, M.; Bauer, P.; Mastromauro, R.A. Charging Infrastructure and Grid Integration for Electromobility. *Proc. IEEE* **2023**, *111*, 371–396. [[CrossRef](#)]
9. Wang, L.; Qin, Z.; Slangen, T.; Bauer, P.; van Wijk, T. Grid Impact of Electric Vehicle Fast Charging Stations: Trends, Standards, Issues and Mitigation Measures—An Overview. *IEEE Open J. Power Electron.* **2021**, *2*, 56–74. [[CrossRef](#)]
10. Rahman, S.; Saha, S.; Islam, S.N.; Arif, M.T.; Mosadeghy, M.; Haque, M.E.; Oo, A.M.T. Analysis of Power Grid Voltage Stability With High Penetration of Solar PV Systems. *IEEE Trans. Ind. Appl.* **2021**, *57*, 2245–2257. [[CrossRef](#)]
11. Flores-Bahamonde, F.; Renaudineau, H.; Llor, A.M.; Chub, A.; Kouro, S. The DC Transformer Power Electronic Building Block: Powering Next-Generation Converter Design. *IEEE Ind. Electron. Mag.* **2023**, *17*, 21–35. [[CrossRef](#)]
12. Fang, J.; Lin, P.; Li, H.; Yang, Y.; Tang, Y. An Improved Virtual Inertia Control for Three-Phase Voltage Source Converters Connected to a Weak Grid. *IEEE Trans. Power Electron.* **2019**, *34*, 8660–8670. [[CrossRef](#)]
13. Luo, W.; Stynski, S.; Chub, A.; Franquelo, L.G.; Malinowski, M.; Vinnikov, D. Utility-Scale Energy Storage Systems: A Comprehensive Review of Their Applications, Challenges, and Future Directions. *IEEE Ind. Electron. Mag.* **2021**, *15*, 17–27. [[CrossRef](#)]
14. Parra, D.; Norman, S.A.; Walker, G.S.; Gillott, M. Optimum community energy storage for renewable energy and demand load management. *Appl. Energy* **2017**, *200*, 358–369. [[CrossRef](#)]
15. Hemmati, R.; Saboori, H. Short-term bulk energy storage system scheduling for load leveling in unit commitment: Modeling, optimization, and sensitivity analysis. *J. Adv. Res.* **2016**, *7*, 360–372. [[CrossRef](#)] [[PubMed](#)]
16. Roberts, B.P.; Sandberg, C. The Role of Energy Storage in Development of Smart Grids. *Proc. IEEE* **2011**, *99*, 1139–1144. [[CrossRef](#)]
17. Lizana, R.; Rivera, S.; Figueroa, F.; Flores-Bahamonde, F.; Rodriguez, J.; Goetz, S.M. Hybrid Energy Storage System Based on a Multioutput Multilevel Converter. *IEEE J. Emerg. Sel. Top. Power Electron.* **2023**, *11*, 3864–3873. [[CrossRef](#)]
18. Dragičević, T.; Lu, X.; Vasquez, J.C.; Guerrero, J.M. DC Microgrids—Part I: A Review of Control Strategies and Stabilization Techniques. *IEEE Trans. Power Electron.* **2016**, *31*, 4876–4891. [[CrossRef](#)]
19. Dragičević, T.; Lu, X.; Vasquez, J.C.; Guerrero, J.M. DC Microgrids – Part II: A Review of Power Architectures, Applications, and Standardization Issues. *IEEE Trans. Power Electron.* **2016**, *31*, 3528–3549. [[CrossRef](#)]
20. Zubieta, L.E. Are Microgrids the Future of Energy?: DC Microgrids from Concept to Demonstration to Deployment. *IEEE Electr. Mag.* **2016**, *4*, 37–44. [[CrossRef](#)]
21. Shen, J.; Khaligh, A. A Supervisory Energy Management Control Strategy in a Battery/Ultracapacitor Hybrid Energy Storage System. *IEEE Trans. Transp. Electr.* **2015**, *1*, 223–231. [[CrossRef](#)]
22. Lukic, S.M.; Wirasingha, S.G.; Rodriguez, F.; Cao, J.; Emadi, A. Power Management of an Ultracapacitor/Battery Hybrid Energy Storage System in an HEV. In Proceedings of the 2006 IEEE Vehicle Power and Propulsion Conference, Windsor, UK, 6–8 September 2006; pp. 1–6. [[CrossRef](#)]
23. Jiang, W.; Zhu, C.; Yang, C.; Zhang, L.; Xue, S.; Chen, W. The Active Power Control of Cascaded Multilevel Converter Based Hybrid Energy Storage System. *IEEE Trans. Power Electron.* **2019**, *34*, 8241–8253. [[CrossRef](#)]
24. Zhang, L.; Tang, Y.; Yang, S.; Gao, F. Decoupled Power Control for a Modular-Multilevel-Converter-Based Hybrid AC–DC Grid Integrated With Hybrid Energy Storage. *IEEE Trans. Ind. Electron.* **2019**, *66*, 2926–2934. [[CrossRef](#)]
25. Abu-Rub, H.; Holtz, J.; Rodriguez, J.; Baoming, G. Medium-Voltage Multilevel Converters—State of the Art, Challenges, and Requirements in Industrial Applications. *IEEE Trans. Ind. Electron.* **2010**, *57*, 2581–2596. [[CrossRef](#)]
26. Dekka, A.; Wu, B.; Zargari, N.R. A Novel Modulation Scheme and Voltage Balancing Algorithm for Modular Multilevel Converter. *IEEE Trans. Ind. Appl.* **2016**, *52*, 432–443. [[CrossRef](#)]
27. Jiang, W.; Zhu, C.; Xue, S.; Ren, K.; Yang, C. DC-Side-Fault-Tolerant Control of a Battery-Supercapacitor Hybrid Energy Storage System Based on Cascaded Multilevel Converter and Auxiliary Power Loop. *IEEE Trans. Ind. Electron.* **2020**, *67*, 7451–7460. [[CrossRef](#)]

28. Jayan, V.; Hussein, A.S.; Ghias, A. Model Predictive Control of Cascaded Multi-Output Multilevel Converter. In Proceedings of the 2019 IEEE International Conference on Industrial Technology (ICIT), Melbourne, VIC, Australia, 13–15 February 2019; pp. 1247–1251. [[CrossRef](#)]
29. Jayan, V.; Ghias, A.M.Y.M. Operational Limits of a Cascaded Dual-Output Multilevel Converter Using Model Predictive Control. *IEEE Trans. Power Electron.* **2021**, *36*, 7026–7037. [[CrossRef](#)]
30. Jayan, V.; Ghias, A. Cascaded Dual Output Multilevel Converter to Enhance Power Delivery and Quality. In Proceedings of the 2019 IEEE Energy Conversion Congress and Exposition (ECCE), Baltimore, MD, USA, 29 September 2019–3 October 2019; pp. 2910–2915. [[CrossRef](#)]
31. Sun, P.; Tian, Y.; Pou, J.; Konstantinou, G. Beyond the MMC: Extended Modular Multilevel Converter Topologies and Applications. *IEEE Open J. Power Electron.* **2022**, *3*, 317–333. [[CrossRef](#)]
32. Goetz, S.M.; Peterchev, A.V.; Weyh, T. Modular Multilevel Converter with Series and Parallel Module Connectivity: Topology and Control. *IEEE Trans. Power Electron.* **2015**, *30*, 203–215. [[CrossRef](#)]
33. Ilves, K.; Taffner, F.; Norrga, S.; Antonopoulos, A.; Harnefors, L.; Nee, H.P. A Submodule Implementation for Parallel Connection of Capacitors in Modular Multilevel Converters. *IEEE Trans. Power Electron.* **2015**, *30*, 3518–3527. [[CrossRef](#)]
34. Li, Z.; Lizana F, R.; Sha, S.; Yu, Z.; Peterchev, A.V.; Goetz, S.M. Module Implementation and Modulation Strategy for Sensorless Balancing in Modular Multilevel Converters. *IEEE Trans. Power Electron.* **2019**, *34*, 8405–8416. [[CrossRef](#)]
35. Li, Z.; Lizana F, R.; Yu, Z.; Sha, S.; Peterchev, A.V.; Goetz, S.M. A Modular Multilevel Series/Parallel Converter for a Wide Frequency Range Operation. *IEEE Trans. Power Electron.* **2019**, *34*, 9854–9865. [[CrossRef](#)]
36. Li, Z.; Lizana, R.; Yu, Z.; Sha, S.; Peterchev, A.V.; Goetz, S.M. Modulation and Control of Series/Parallel Module for Ripple-Current Reduction in Star-Configured Split-Battery Applications. *IEEE Trans. Power Electron.* **2020**, *35*, 12977–12987. [[CrossRef](#)]
37. Lizana F, R.; Rivera, S.; Li, Z.; Dekka, A.; Rosenthal, L.; Bahamonde I., H.; Peterchev, A.V.; Goetz, S.M. Modular Multilevel Series/Parallel Converter for Bipolar DC Distribution and Transmission. *IEEE J. Emerg. Sel. Top. Power Electron.* **2021**, *9*, 1765–1779. [[CrossRef](#)]
38. Jacobs, K.; Heinig, S.; Johannesson, D.; Norrga, S.; Nee, H.P. Comparative Evaluation of Voltage Source Converters With Silicon Carbide Semiconductor Devices for High-Voltage Direct Current Transmission. *IEEE Trans. Power Electron.* **2021**, *36*, 8887–8906. [[CrossRef](#)]
39. Dekka, A.; Beik, O.; Narimani, M. Modulation and Voltage Balancing of a Five-Level Series-Connected Multilevel Inverter With Reduced Isolated Direct Current Sources. *IEEE Trans. Ind. Electron.* **2020**, *67*, 8219–8230. [[CrossRef](#)]

Disclaimer/Publisher’s Note: The statements, opinions and data contained in all publications are solely those of the individual author(s) and contributor(s) and not of MDPI and/or the editor(s). MDPI and/or the editor(s) disclaim responsibility for any injury to people or property resulting from any ideas, methods, instructions or products referred to in the content.